npj | 2D Materials and Applications

www.nature.com/npj2dmaterials

ARTICLE OPEN

Black phosphorus: a two-dimensional reductant for in situ nanofabrication

Hao Huang[1,3], Quanlan Xiao[1,2], Jiahong Wang[1], Xue-Feng Yu[1], Huaiyu Wang[1], Han Zhang[2] and Paul K. Chu[3]

The reducing capability of two-dimensional black phosphorus is demonstrated. The high reducing ability and unique two-dimensional morphology of black phosphorus not only facilitate in situ synthesis of Au nanoparticles and BP@Au composites, but also enable multiscale control of local reduction of GO to reduced GO (rGO). The novel two-dimensional reductant has large potential in various in situ nanofabrication applications.

npj 2D Materials and Applications (2017)1:20 ; doi:10.1038/s41699-017-0022-6

INTRODUCTION

Two-dimensional (2D) materials with an ultrathin layered structure have many unique properties and applications.[1, 2] For instance, graphene boasting good optoelectronic characteristics and high mechanical strength has large potential in energy conversion and storage[3–5] and transition-metal dichalcogenides (TMDs) with unique semiconducting properties are attractive to scalable digital field-effect transistors.[6–8] Furthermore, the chemical reactivity of 2D materials such as graphene oxide (GO) and TMDs has raised concerns and novel templates have been proposed to fabricate functional composites.[9–17]

Black phosphorus (BP) has emerged to be an exciting member of the 2D family.[18, 19] BP has strong in-plane bonds in conjunction with weak van der Waals interlayer interactions thereby enabling exfoliation into few-layer BP sheets or phosphorene (single-layer BP).[20–24] Since 2014, BP has attracted tremendous research interest[25–38] because of its unique properties such as layer-dependent direct bandgap,[28, 39] anisotropy,[25, 26, 31, 32, 34, 40] hinge-like structure,[41] and quasi-one-dimensional excitonicnature,[42] all of which contrast markedly with those of other types of 2D materials. Nevertheless, BP degrades under ambient conditions as a result of the reaction with oxygen ($P \rightarrow P_xO_y$) and subsequent transformation to PO_4^{3-} in the presence of water.[43] Degradation leads to compromised electronic and optical performance and has generally been considered a serious obstacle hampering the application of BP.[38, 44] On the other hand, the high chemical reactivity of BP with respect to oxidation may be exploited and in the work, we investigate the reducibility of BP. Synthesis of nanomaterials generally involves chemical reduction with an extrinsic organic or inorganic reagent as the reductant. Considering the unique 2D structure and high chemical reactivity of BP, it may be an efficient 2D reductant in nanomaterials synthesis. Herein, we demonstrate that BP sheets serve as a reductant in the synthesis of Au nanoparticles and BP@Au composites and provide multiscale control of local GO reduction. This new application not only enables fabrication of various functional composites comprising 2D materials, but also extends the application of 2D materials to new areas.

RESULTS AND DISCUSSION

The BP sheets are synthesized by a modified *N*-methyl-2-pyrrolidone (NMP) solvent exfoliation method reported by our group previously.[24] The BP dispersion is centrifuged at different speeds to obtain BP sheets with a relatively uniform size. The sheets in the supernatant after centrifugation at 7000 rpm are named BP_{7000}. The precipitate collected by centrifugation at 7000 rpm is re-dispersed in NMP and the sheets labelled as BP_{4000} are obtained from the supernatant after centrifugation at 4000 rpm. Subsequently, the suspension with the precipitate after centrifugation at 4000 rpm is centrifuged one more time at 1000 rpm to obtain the BP sheets designated BP_{1000}.

The scanning electronic microscopy (SEM) and *inset* atomic force microscopy (AFM) images in Fig. 1a show that the BP_{7000} sheets have an average diameter of about 500 ± 100 nm and thickness of about 18 ± 2 nm. No obvious bubbles can be observed from the surface as shown in the high-magnification AFM image (Fig. S1), indicating that there is no significant oxidation of the as-prepared BP sheets. The transmission electron microscopy (TEM) image in Fig. 1b shows the typical layered morphology of one of the sheets and the high-resolution TEM (HR-TEM) image in the inset reveals clear lattice fringes of 2.54 and 2.85 Å ascribed to the (111) and (004) planes of the BP crystal, respectively.[21, 45] The extinction spectrum acquired from the NMP solution of the BP_{7000} sheets in Fig.1c shows a broad extinction band spanning the ultraviolet and near-infrared regions producing the fawn color in the solution. Raman scattering is performed to characterize the BP sheets further. As shown in Fig. 1d, three prominent peaks corresponding to the A^1_g, B_{2g}, and A^2_g modes of BP sheets exhibit slight blue-shifts in comparison with bulk BP due to the small thickness.[24] The results demonstrate successful synthesis of BP sheets by the NMP solvent exfoliation method. It is noted that larger BP sheets with a lateral size up to 5 μm (BP_{4000}) and 40 μm (BP_{1000}) can be obtained by centrifugation at 4000 and 1000 rpm, respectively (Fig. S2).

The reducibility of BP is assessed. Since synthesis of metal particles generally involves chemical reduction of the corresponding metal salt with an external reductant, the BP sheets are used

[1]Institute of Biomedicine and Biotechnology, Shenzhen Institutes of Advanced Technology, Chinese Academy of Sciences, Shenzhen 518055, People's Republic of China; [2]College of Optoelectronic Engineering, Shenzhen University, Shenzhen 518060, People's Republic of China and [3]Department of Physics and Materials Science, City University of Hong Kong, Tat Chee Avenue, Kowloon, Hong Kong, China
Correspondence: Xue-Feng Yu (xf.yu@siat.ac.cn) or Paul K. Chu (paul.chu@cityu.edu.hk)

Received: 20 July 2016 Revised: 21 September 2016 Accepted: 25 October 2016
Published online: 04 July 2017

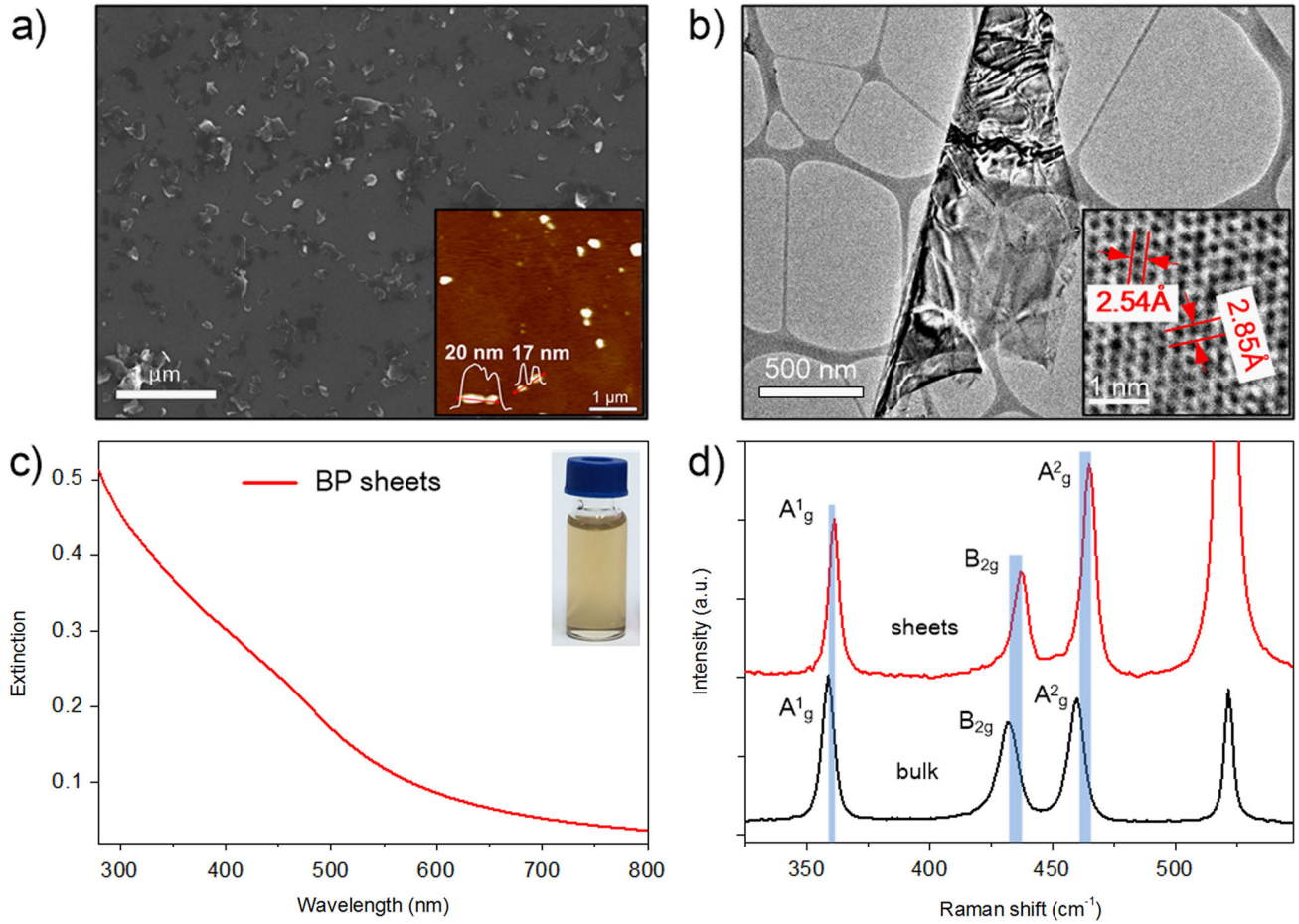

Fig. 1 Characterization of BP_{7000} sheets. **a** SEM image with AFM image and height profiles shown in the inset; **b** TEM image and HR-TEM image (*inset*) of one sheet; **c** Extinction spectrum with photograph of the BP sheets dispersed in NMP shown in the *inset*; **d** Raman scattering spectra acquired from the BP sheets and bulk crystalline BP

as the reductant in the synthesis of Au nanoparticles as illustrated in Fig. 2a. When $HAuCl_4$ is added to the aqueous solution containing the BP_{7000} sheets, the colour turns from fawn to red within 5 min (inset image in Fig. 2b). Correspondingly, a surface plasmon resonance (SPR) band appears at about 540 nm (Fig. 2b). The TEM image of the products in Fig. 2c verifies successful synthesis of Au nanoparticles with an average size of 28 ± 10 nm indicating the occurrence of a redox reaction in which Au^{3+} is reduced to Au atoms. The reducing ability of the BP_{4000} sheets and BP_{7000} sheets is compared. As shown in Fig. S3a, the BP_{4000} sheets have more scattering than the BP_{7000} sheets according to the larger size of BP_{4000}. In the reduction reaction, the Au nanoparticles synthesized with BP_{7000} exhibit a larger SPR band around 540 nm than BP_{4000} (Fig. S3b), suggesting the stronger reducing ability of the BP_{7000} sheets.

To study the mechanism of the reduction reaction, control experiments are performed and the results are shown in Fig. S4. When $HAuCl_4$ reacts with NMP and water, no Au SPR band can be observed thus excluding possible reducibility of the residual NMP in the BP solution. Furthermore, when $HAuCl_4$ and BP are mixed in the NMP solution without water, no Au nanoparticles are synthesized, demonstrating the necessity of H_2O in the reduction. It can be inferred that the BP sheets can reduce Au^{3+} into Au nanoparticles in the presence of H_2O.

An in situ reduction reaction is carried out to directly observe the reducibility of a BP sheet (Fig. 2d–g). One large BP sheet with a microscale lateral size up to 40 μm is placed on a Si_3N_4/Si substrate. After one drop of the aqueous solution containing $HAuCl_4$ is introduced, the reduction reaction occurs immediately. Within 1 min, the BP sheet fades while Au nanoparticles are synthesized (Watch the video clip in the Supporting Materials for the dynamic process). Excess water can lead to complete degradation of the BP sheets and no BP sheets can be observed in Fig. 2c. The Au nanoparticles are mainly concentrated along the edges of the sheet probably due to the higher reactivity of the edge defects[9] and aggregation of naked Au nanoparticles without a surfactant. Although various reducing agents have been proposed in the synthesis of metal nanoparticles, the use of 2D BP as the reductant has not been demonstrated. Since the reduction reaction is fast and a high temperature is not required and this synthetic strategy has many advantages.

The reduction process can be regulated to tailor the products. Figure 3a shows a typical example of the synthesis of the BP@Au composites. In brief, 300 μL of the water solution containing $HAuCl_4$ are added to the NMP solution containing the BP_{7000} sheets. The mixture is stirred for 1 h to enable in situ growth of Au nanoparticles on the BP sheets. Figure 3b, c display the morphology of the BP@Au products showing Au nanoparticles with an average size of 23 ± 8 nm on the BP sheets. Figure 3d presents the HR-TEM images of a BP@Au composite and Fig. 3e discloses lattice fringes of 2.37 and 2.55 Å corresponding to the Au (111) plane and BP (111) plane, respectively.[45, 46] It is noted that different products are obtained from the reactions illustrated in Fig. 2a and Fig. 3a due to the different reaction conditions. In brief, the amount of H_2O plays an important role in the balance between the growth of Au nanoparticles and degradation of BP

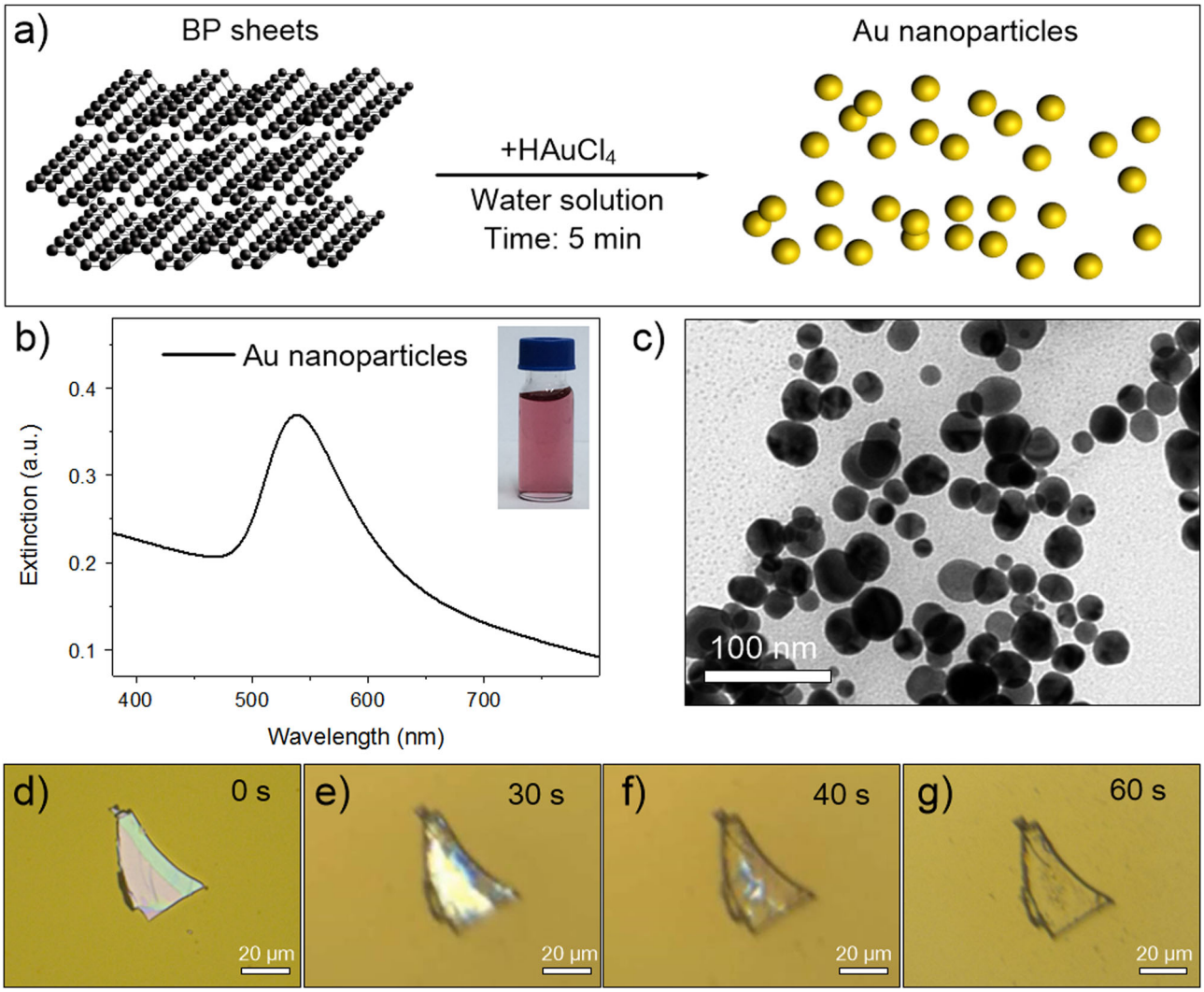

Fig. 2 **a** Schematic illustration of the synthesis of Au nanoparticles using BP sheets as the reductant; **b** Extinction spectrum with the photograph of the solution shown in the *inset*; **c** TEM image of the synthesized Au nanoparticles; **d**–**g** Reflection microscopy images demonstrating in situ synthesis of Au nanoparticles using BP sheets

during the reaction. In the reaction shown in Fig. 2a, the reaction takes place in water and excess water leads to complete degradation of BP during the reaction. With regard to the reaction shown in Fig. 3a, it takes place in NMP with a limited amount of water thus resulting in the growth of Au nanoparticles on the BP surface.

The chemical composition of the bare BP sheets and BP@Au composites is determined by X-ray photoelectron spectroscopy (XPS). Figure 4a shows the P2p3/2 and P2p1/2 doublet at 129.6 and 130.4 eV, respectively, characteristic of crystalline BP. A small oxidized phosphorus (P_xO_y) sub-band is apparent at ~133.7 eV as a result of unavoidable sample processing. Figure 4b shows no detectable Au signals from the bare BP sheets. Figure 4c shows that the BP@Au composites exhibit the same P2p3/2, P2p1/2 doublet and P_xO_y sub-band, indicating that the Au nanoparticles on the BP sheets do not change the crystallinity of BP. Figure 4d shows Au4f5/2 and Au4f7/2 core level peaks at 88.2, 87.3, 84.3, and 83.5 eV, all of which are slightly shifted in comparison with bulk Au probably due to the Au-BP interaction.[9, 47] Figure S5 depicts the Raman scattering spectrum of the BP@Au composites. Compared to the bare BP sheets, the BP@Au composites show a larger intensity ratio of the A^1_g to B_{2g} mode and red-shifts of the three prominent peaks ascribed to the Au–BP interaction. The above results demonstrate successful synthesis of the BP@Au composites in which the BP sheets maintain the morphology and crystal quality. It should be noted that the growth of Au nanoparticles cannot improve the stability of the BP sheets (see Fig. S6), and further modification is required to enhance the stability.[29]

Extinction spectra are acquired from the BP@Au composites. As shown in Fig. S7, the 535 nm SPR band is observed and the solution changes colour after the reaction. The change in scattering compared to BP sheets is probably due to the appearance of Au nanoparticles on the BP surface. In addition, in comparison with the sample in Fig. 2, the smaller Au nanoparticles give rise to a shorter SPR peak wavelength.

The amount of water influences the reaction. If the amount of water is increased to 1 mL, growth of Au nanoparticles is concomitant with serious degradation of the BP sheets (see Fig. S8) and a similar phenomenon has been reported.[40] The results demonstrate that the BP@Au composites can be synthesized by controlling BP-induced reduction in which only a portion of the outer BP reduces Au^{3+} to Au nanoparticles in situ. It is known that good contact with the metal is critical to semiconducting 2D materials in order to inject carriers into the conduction or valence band of a device. The protocol demonstrated by the

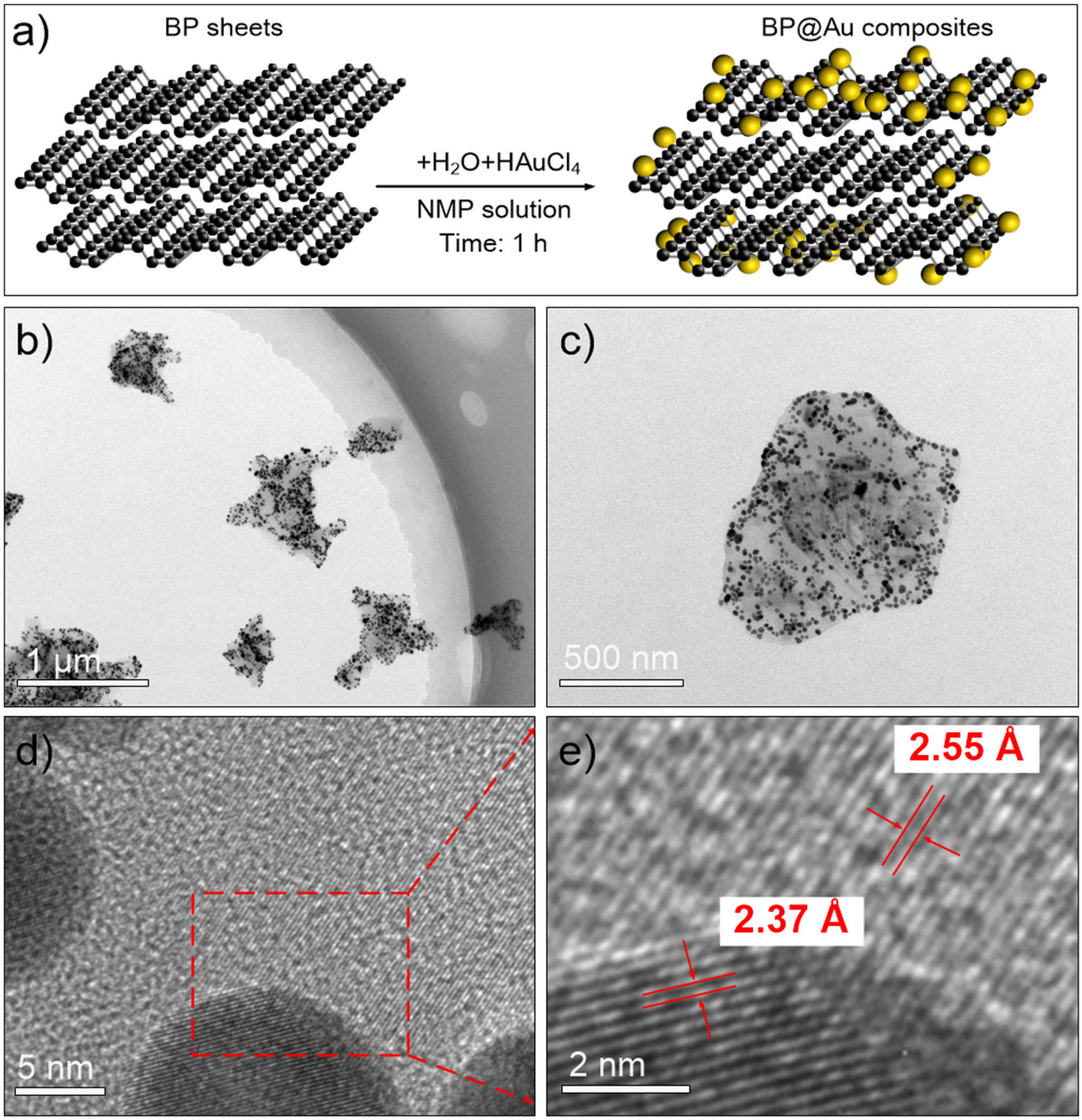

Fig. 3 **a** Schematic illustration of synthesis of BP@Au composites by controlling BP-induced reduction; **b**, **c** TEM images of the BP@Au composites; **d**, **e** HR-TEM images of the BP@Au composites

synthesis of BP@Au composites can be further adopted to investigate BP-metal interactions.

Considering the unique 2D morphology of BP compared to other common reducing agents, the BP sheets are further applied to nanofabrication. One such application is in situ reduction of GO to reduced-GO (rGO), which is important and challenging.[16] GO sheets are synthesized by the method demonstrated by Gao et al.[48] The weak shoulder at ~300 nm (n-π* transitions of the carbonyl groups) in Fig. S9a indicates successful synthesis of GO. Herein, a drop of the water solution containing the GO sheets is spin-coated on a coverslip to fabricate a GO film (Fig. S9b, c). Figure 5a illustrates the local reduction process of GO by BP. In brief, the BP_{1000} sheet is placed on a GO film and then kept in air at a relative humidity of 60% at 50 °C for 48 h. Owing to the high reducing ability of BP, the GO in the area covered by the BP sheets are gradually reduced to rGO producing a microscale-reduced GO film. The reflection microscopy images in Fig. 5b clearly show the 40 μm-scale reduced area on the GO film. The four points indicated in Fig. 5b are further characterized by Raman scattering. All four areas exhibit the two characteristic bands of disordered carbon, namely the D band at 1330 cm^{-1} and G band at 1590 cm^{-1} (Fig. 5c, d),[49] but the D to G band intensity ratios (I_D/I_G) are different. The I_D/I_G ratios of 1.18 and 1.19 and calculated from R1 and R2 in the rGO area are larger than those of 0.99 and 0.98 from points G1 and G2 around the GO area. The I_D/I_G ratio is commonly used to evaluate the degree of structural disorder and defects and increase in I_D/I_G is an indicator of GO reduction.[49, 50] Here, the different I_D/I_G ratios provide evidence about successful reduction

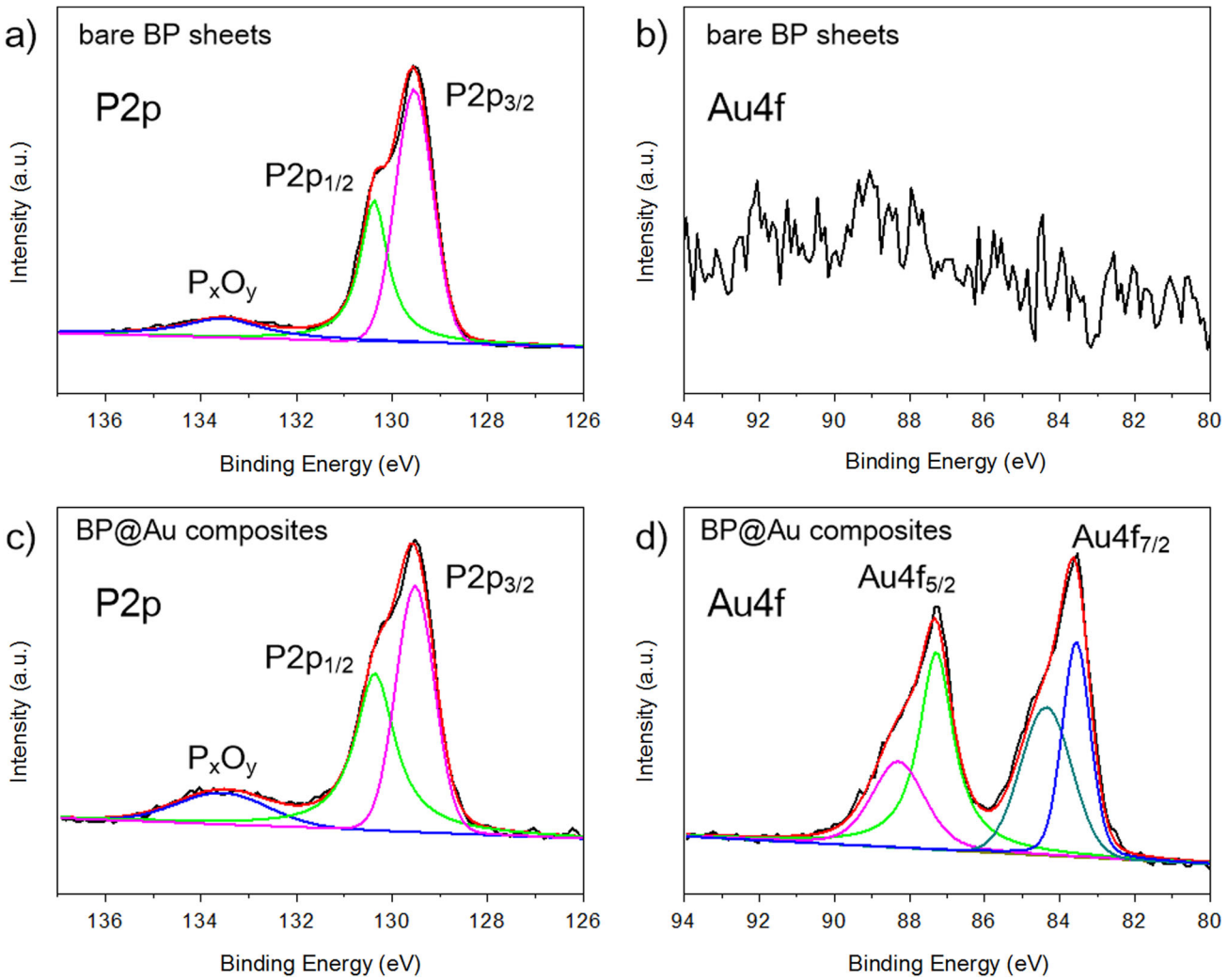

Fig. 4 **a** XPS P2p and **b** Au4f peaks of the BP sheets as well as **c** P2p and **d** Au4f peaks of the BP@Au composites, together with the best fits of the individual components

of GO to rGO by the BP sheet. Furthermore, Fig. 5e shows the I_D/I_G ratios obtained from the Raman map of the BP reduced area and the uniform bright yellow region reveals the smooth transition from GO to rGO.

Since the size of the BP products can be regulated, the reduction reaction can be extended to different scales. As shown in Fig. S10, a GO film with 5 μm-scale rGO areas can be fabricated by using the BP_{4000} sheets as the reductant. On the other hand, by using BP powders as the reductant, a GO film with a macroscale rGO area can instead be fabricated in 3 h. Figure 5f depicts the photograph of a typical rGO "SIAT" pattern on the GO film. The "SIAT" pattern shows black and light yellow contrast with the black areas being rGO and light yellow areas intact with GO, demonstrating that this is a simple and efficient means to accomplish multiscale control in local GO reduction. The XPS survey scans of the black and light yellow areas are shown in Fig. 5g. The survey scans highlight the O1s and C1s peaks while the O1s peak decreases vastly in the reduced areas, further confirming BP-induced reduction of GO to rGO.

To demonstrate the role of H_2O and BP in the reduction more clearly, reactions under different humidity conditions are carried out. As shown in Fig. S11, the GO film reduced by the BP powder at humidity of 30% at 50 °C has an I_D/I_G ratio of 1.03 in the reduced areas, while a large I_D/I_G ratio of 1.16 is obtained from the areas reduced at humidity of 60% at 50 °C. It is known that GO cannot be reduced by H_2O at a low temperature of 50 °C and hence, the results indicate that reduction of GO stems from co-operation of H_2O and BP. Furthermore, the reaction time is taken into consideration. Figure S12a, b show the time dependent I_D/I_G ratios of the areas reduced by the BP_{1000} sheet and BP powder, respectively. In the BP_{1000} sheet reduction, the I_D/I_G ratio changes from 12 h and reaches a relative stable value of about 1.18 after 48 h. In the BP powder reduction, the I_D/I_G ratio changes from 0.5 h and reaches a relative stable value of about 1.18 after 3 h. The smaller reduction time needed by the BP powder is due to the larger amount of BP.

Additional experiments show that the reduction degree can be regulated by terminating the reduction reaction by moving the BP sheet aside after the reaction for 24 h. The reflection microscope image in Fig. S13 shows the profiles of the reduced area and BP sheet aside. In this case, just a slight increase in the I_D/I_G ratios (from 1.0 to 1.06) is observed after reduction, implying that only the upper GO layers have been reduced to rGO. These results confirm the controllability of the BP-induced reduction reaction.

CONCLUSION

The reducing capability of 2D BP is demonstrated. The high reducing ability and unique 2D morphology not only facilitate in situ synthesis of Au nanoparticles and BP@Au composites, but

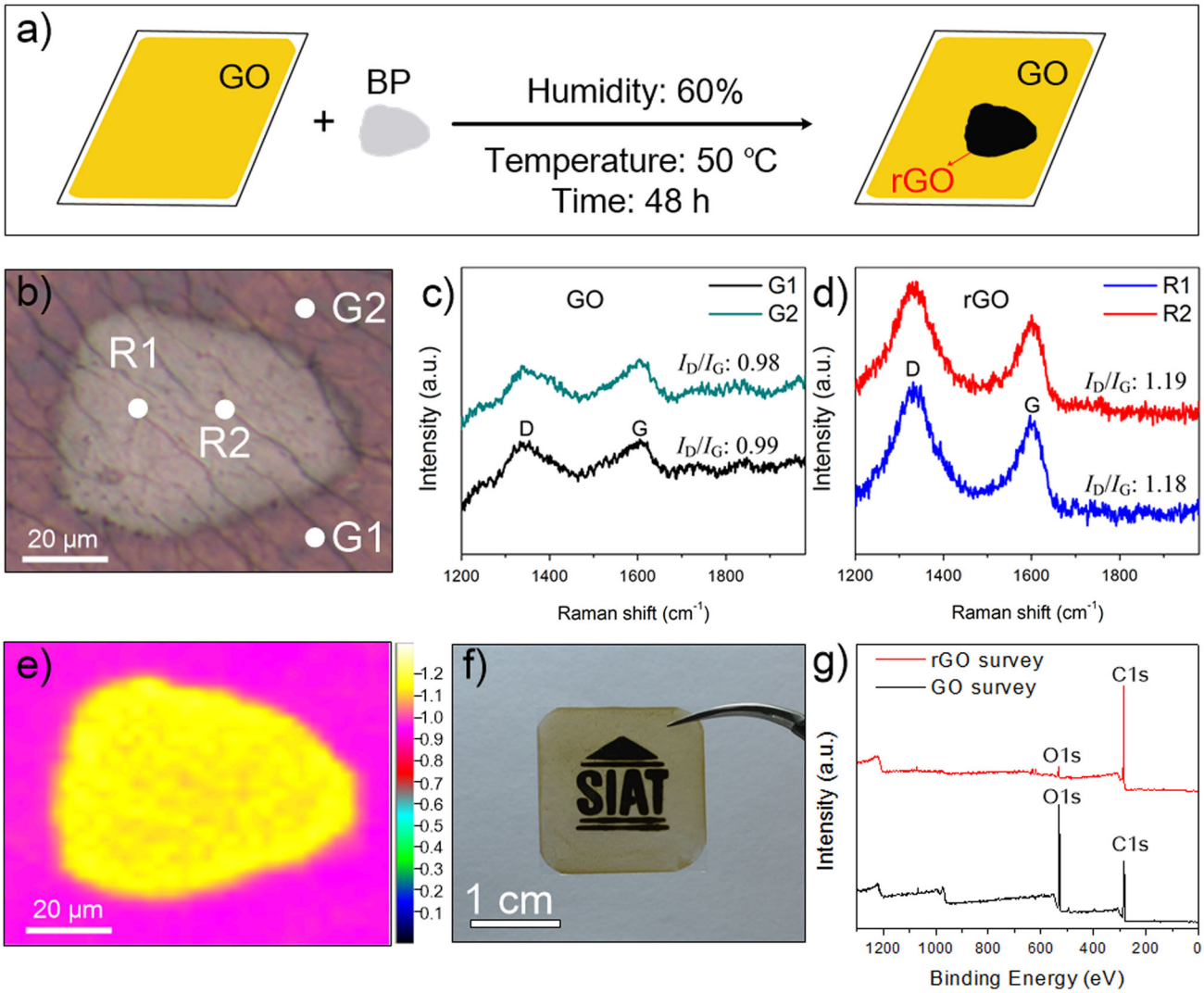

Fig. 5 **a** Schematic illustration of BP-induced local reduction of the GO film; **b** Reflection microscopy image of a microscale rGO pattern on the GO film; **c**, **d** Raman scattering spectra and corresponding I_D/I_G ratios of the GO areas **c** and rGO areas **d** indicated in **b**; **e** Raman map of the I_D/I_G ratios for the microscale reduced area on the GO film; **f** Photograph of a rGO "SIAT" pattern on a GO film. **g** XPS survey scans of the GO areas and rGO areas in **e**

also enable multiscale control in local reduction of GO to rGO. The novel 2D reductant has large potential in various in situ nanofabrication applications and this study also provides better understanding of the exciting properties of BP and how they can be exploited in practice.

METHODS

Materials

The BP crystals were purchased from a commercial supplier (Smart-Elements) and stored in a dark Ar glove box. NMP (99.5%, anhydrous) and graphite (45 μm) were purchased from Aladdin Reagents, chloroauric acid ($HAuCl_4{\cdot}4H_2O$, 99.99%), H_2SO_4 (95 ~ 98%) were bought from Sinopharm Chemical Reagent Co. Ltd. (Shanghai, China), and K_2FeO_4 was obtained from Hubei CSW-China Chemistry Co. Ltd. All the chemicals used in this study were analytical reagent grade and used without further purification. Ultrapure water (18.25 MΩ cm^{-1}, 25 °C) was used to prepare the solutions.

Synthesis of BP sheets

The BP sheets were prepared by a simple liquid exfoliation method utilizing bath sonication. The bulk BP (40 mg) powder was immersed in 40 mL of the NMP solution and sonicated in an ice water bath for 4 h with a power of 300 W. Afterwards, it was centrifuged at 7000 rpm for 10 min and the supernatant contained the BP sheets with a lateral size of about 500 ± 100 nm named BP_{7000}. To obtain BP sheets up to 5 μm, the precipitate was re-dispersed in NMP followed by centrifuging at 4000 rpm for another 10 min and the supernatant contained larger BP sheets designated as BP_{4000}. To obtain larger BP sheets up to 40 μm, the precipitate was re-dispersed in NMP followed by centrifuging at 1000 rpm for another 10 min and the supernatant contained larger BP sheets named BP_{1000}.

BP-induced reduction of Au^{3+} to Au nanoparticles

One milliliter of the NMP solution containing the BP_{7000} sheets was centrifuged at 12,000 rpm for 15 min and the precipitate was re-dispersed in 1 mL H_2O. Immediately thereafter, 1 mL of an aqueous solution containing 2.5×10^{-6} mol $HAuCl_4$ was added. After stirring lightly for 5 min, the color changed from light yellow to purple red indicating successful synthesis of Au nanoparticles.

BP-induced synthesis of BP@Au composites

The amount of water and reaction time were carefully adjusted to control the reaction. Typically, 700 μL of NMP and 300 μL of the aqueous solution

containing 2.5×10^{-6} mol $HAuCl_4$ were added to 1 mL of the NMP solution containing the BP_{7000} sheets. After stirring lightly for 1 h, it was centrifuged at 12,000 rpm for 10 min to remove excess $HAuCl_4$ and water and the precipitate was re-dispersed in the NMP solution.

Synthesis of GO sheets and GO films

The GO sheets were synthesized according to the procedures described previously.[48] Succinctly speaking, 100 mg of graphite flakes were added to the reactor containing 40 mL of concentrated H_2SO_4 and 5 g of K_2FeO_4 and stirred for 2 h at room temperature. It was centrifuged at 10,000 rpm for 3 min to remove the H_2SO_4 and the precipitate was purified by repetitive water rinsing and centrifugation until the pH was 7. The GO film was prepared by spin-coating 400 µL of the 0.5 mg/mL GO solution on a 1.8 cm × 1.8 cm coverslip.

BP-induced reduction of GO film

To fabricate the 40 µm-scale rGO pattern, 1 mL of the NMP solution containing the BP_{1000} sheets was centrifuged at 4000 rpm for 10 min and the precipitate was re-dispersed in 10 mL of ethanol. Immediately thereafter, 10 µL of the ethanol solution containing the BP_{1000} was dropped onto a GO film and the film was aged at 50 °C and 60% relative humidity for 48 h. The film was then rinsed with ultrapure water to remove excess BP sheets. To fabricate the macroscale rGO pattern, a hollow "SIAT" template was covered on the GO film and filled with BP powders. The film was kept at 50 °C and 60% relative humidity for 3 h. Afterwards, the film was rinsed with ultrapure water.

Characterization

SEM was carried out on the ZEISS SUPRA 55 (Carl Zeiss, Germany) field-emission scanning electron microscope and the TEM and HR-TEM images were taken on the FEI Tecnai G2 F30 transmission electron microscope at an acceleration voltage of 200 kV. AFM was performed on the drop-cast flakes on Si substrates on the MFP-3D-S atomic force microscope (Asylum Research, USA) using the AC mode (tapping mode) in air. Raman scattering was conducted on a Horiba Jobin-Yvon LabRam HR-VIS high-resolution confocal Raman microscope equipped with a 633 nm laser as the excitation source at room temperature. The UV–Vis–NIR extinction spectra were recorded on a Lambda25 spectrophotometer (PerkinElmer) using QS-grade quartz cuvettes at room temperature. XPS was conducted on the Thermo Fisher ESCALAB 250XiXPS. The reflection images were taken by the VHX-2000C digital microscope (Keyence, Japan) and the transmission images were acquired by fluorescence microscopy.

ACKNOWLEDGEMENTS

This work was jointly supported by the National Natural Science Fund of China No. 51672305, Frontier Research Key Project of the Chinese Academy of Sciences No. QYZDB-SSW-SLH034, Shenzhen Science and Technology Research Funding No. JCYJ201602293000503, Leading Talents of Guangdong Province Program No. 00201520, and Hong Kong Research Grants Council (RGC) General Research Funds (GRF) No. 11301215.

AUTHOR CONTRIBUTIONS

H.H., Q.X. and J.W. conducted the experiments and determined the measurements; H. W., H.Z. discussed the data and provided some useful suggestions; X.Y. and P.C. supervised and directed the project; all of the authors read and contributed to the paper.

ADDITIONAL INFORMATION

Supplementary Information accompanies the paper on the *npj 2D Materials and Applications* website (doi:10.1038/s41699-017-0022-6).

Competing interests: The authors declare no competing financial interests.

Publisher's note: Springer Nature remains neutral with regard to jurisdictional claims in published maps and institutional affiliations.

REFERENCES

1. Xu, M., Liang, T., Shi, M. & Chen, H. Graphene-like two-dimensional materials. *Chem. Rev.* **113**, 3766–3798 (2013).
2. Koski, K. J. & Cui, Y. The new skinny in two-dimensional nanomaterials. *ACS Nano* **7**, 3739–3743 (2013).
3. Bao, Q. et al. Broadband graphene polarizer. *Nat. Photon.* **5**, 411–415 (2011).
4. Lee, C., Wei, X., Kysar, J. W. & Hone, J. Measurement of the elastic properties and intrinsic strength of monolayer grapheme. *Science* **321**, 385–388 (2008).
5. Novoselov, K. S. et al. Electric field effect in atomically thin carbon films. *Science* **306**, 666–669 (2004).
6. Chhowalla, M. et al. The chemistry of two-dimensional layered transition metal dichalcogenide nanosheets. *Nat. Chem* **5**, 263–275 (2013).
7. Zou, X. M. et al. Interface engineering for high-performance top-gated MoS_2 field-effect transistors. *Adv. Mater.* **26**, 6255–6261 (2014).
8. Wang, Q. H., Kalantar-Zadeh, K., Kis, A., Coleman, J. N. & Strano, M. S. Electronics and optoelectronics of two-dimensional transition metal dichalcogenides. *Nat. Nanotechnol* **7**, 699–712 (2012).
9. Shi, Y. et al. Selective decoration of Au nanoparticles on monolayer MoS_2 single crystals. *Sci. Rep* **3**, 1839 (2013).
10. Sreeprasad, T. S., Nguyen, P., Kim, N. & Berry, V. Controlled, defect-guided, metal-nanoparticle incorporation onto MoS_2 via chemical and microwave routes: electrical, thermal, and structural properties. *Nano Lett.* **13**, 4434–4441 (2013).
11. Sarkar, D. et al. Functionalization of transition metal dichalcogenides with metallic nanoparticles: Implications for doping and gas-sensing. *Nano Lett.* **15**, 2852–2862 (2015).
12. Chen, X. et al. Synthesis of "clean" and well-dispersive Pd nanoparticles with excellent electrocatalytic property on graphene oxide. *J. Am. Chem. Soc.* **133**, 3693–3695 (2011).
13. Huang, X. et al. Solution-phase epitaxial growth of noble metal nanostructures on dispersible single-layer molybdenum disulfide nanosheets. *Nat. Commun.* **4**, 1444 (2013).
14. Chen, J. et al. One-pot synthesis of CdS nanocrystals hybridized with single-layer transition-metal dichalcogenide nanosheets for efficient photocatalytic hydrogen evolution. *Angew. Chem. Int. Ed.* **54**, 1210–1214 (2015).
15. Ocsoy, I. et al. DNA-guided metal-nanoparticle formation on graphene oxide surface. *Adv. Mater.* **25**, 2319–2325 (2013).
16. Wei, Z. et al. Nanoscale tunable reduction of graphene oxide for graphene electronics. *Science* **328**, 1373–1376 (2010).
17. Chen, S., Zhu, J., Wu, X., Han, Q. & Wang, X. Graphene oxide-MnO_2 nanocomposites for supercapacitors. *ACS Nano* **4**, 2822–2830 (2010).
18. Churchill, H. O. & Jarillo-Herrero, P. Two-dimensional crystals: Phosphorus joins the family. *Nat. Nanotechnol* **9**, 330–331 (2014).
19. Liu, H., Du, Y., Deng, Y. & Ye, P. D. Semiconducting black phosphorus: synthesis, transport properties and electronic applications. *Chem. Soc. Rev.* **44**, 2732–2743 (2015).
20. Brent, J. R. et al. Production of few-layer phosphorene by liquid exfoliation of black phosphorus. *Chem. Commun.* **50**, 13338–13341 (2014).
21. Yasaei, P. et al. High-quality black phosphorus atomic layers by liquid-phase exfoliation. *Adv. Mater.* **27**, 1887–1892 (2015).
22. Zhang, X. et al. Black phosphorus quantum dots. *Angew. Chem. Int. Ed.* **54**, 3653–3657 (2015).
23. Kang, J. et al. Solvent exfoliation of electronic-grade, two-dimensional black phosphorus. *ACS Nano* **9**, 3596–3604 (2015).
24. Guo, Z. et al. From black phosphorus to phosphorene: basic solvent exfoliation, evolution of Raman scattering, and applications to ultrafast photonics. *Adv. Funct. Mater.* **25**, 6996–7002 (2015).
25. Li, L. et al. Black phosphorus field-effect transistors. *Nat. Nanotechnol* **9**, 372–377 (2014).
26. Liu, H. et al. Phosphorene: an unexplored 2D semiconductor with a high hole mobility. *ACS Nano* **8**, 4033–4041 (2014).
27. Sun, J. et al. A phosphorene–graphene hybrid material as a high-capacity anode for sodium-ion batteries. *Nat. Nanotechnol* **10**, 980–985 (2015).
28. Zhang, S. et al. Extraordinary photoluminescence and strong temperature/angle-dependent Raman responses in few-layer phosphorene. *ACS Nano* **8**, 9590–9596 (2014).
29. Zhao, Y. et al. Surface coordination of black phosphorus for robust air and water stability. *Angew. Chem.* **128**, 5087–5091 (2016).
30. Hanlon, D. et al. Liquid exfoliation of solvent-stabilised few-layer black phosphorus for applications beyond electronics. *Nat. Commun.* **6**, 8563 (2015).
31. Xia, F. N., Wang, H. & Jia, Y. C. Rediscovering black phosphorus as an anisotropic layered material for optoelectronics and electronics. *Nat. Commun.* **5**, 4458 (2014).
32. Fei, R. X. & Yang, L. Strain-engineering the anisotropic electrical conductance of few-layer black phosphorus. *Nano Lett.* **14**, 2884–2889 (2014).

33. Jia, J. Y. et al. Plasma-treated thickness-controlled two-dimensional black phosphorus and its electronic transport properties. *ACS Nano* **9**, 8729–8736 (2015).
34. Buscema, M. et al. Fast and broadband photoresponse of few-layer black phosphorus field-effect transistors. *Nano Lett.* **14**, 3347–3352 (2014).
35. Engel, M., Steiner, M. & Avouris, P. Black phosphorus photodetector for multispectral, high-resolution imaging. *Nano Lett.* **14**, 6414–6417 (2014).
36. Wang, H. et al. Black phosphorus radio-frequency transistors. *Nano Lett.* **14**, 6424–6429 (2014).
37. Sun, Z. B. et al. Ultrasmall black phosphorus quantum dots: Synthesis and use as photothermal agents. *Angew. Chem. Int. Ed.* **127**, 11688–11692 (2015).
38. Pei, J. et al. Producing air-stable monolayers of phosphorene and their defect engineering. *Nat. Commun.* **7**, 10450 (2016).
39. Tran, V., Soklaski, R., Liang, Y. & Yang, L. Layer-controlled band gap and anisotropic excitons in few-layer black phosphorus. *Phys. Rev. B* **89**, 235319 (2014).
40. Favron, A. et al. Photooxidation and quantum confinement effects in exfoliated black phosphorus. *Nat. Mater.* **14**, 826–832 (2015).
41. Qin, G. Z. et al. Hinge-like structure induced unusual properties of black phosphorus and new strategies to improve the thermoelectric performance. *Sci. Rep* **4**, 6946 (2014).
42. Xu, R. et al. Extraordinarily bound quasi-one-dimensional trions in two-dimensional phosphorene atomic semiconductors. *ACS Nano* **10**, 2046–2053 (2016).
43. Island, J. O., Steele, G. A., Zant, H. S. Jvander & Castellanos-Gomez, A. Environmental instability of few-layer black phosphorus. *2D Mater* **2**, 011002 (2015).
44. Kim, J. S. et al. Toward air-stable multilayer phosphorene thin-films and transistors. *Sci. Rep* **5**, 8989 (2015).
45. Hultgren, R., Gingrich, N. S. & Warren, B. E. The atomic distribution in red and black phosphorus and the crystal structure of black phosphorus. *J. Chem. Phys.* **3**, 351 (1935).
46. Huang, X. et al. Synthesis of hexagonal close-packed gold nanostructures. *Nat. Commun.* **2**, 292 (2011).
47. Takahiro, K. et al. Core level and valence band photoemission spectra of Au clusters embedded in carbon. *J. Appl. Phys.* **100**, 084325 (2006).
48. Peng, L. et al. An iron-based green approach to 1-h production of single-layer graphene oxide. *Nat. Commun.* **6**, 5716 (2015).
49. Moon, I. K., Lee, J., Ruoff, R. S. & Lee, H. Reduced graphene oxide by chemical graphitization. *Nat. Commun.* **1**, 73 (2010).
50. Ferrari, A. C. & Robertson, J. Interpretation of Raman spectra of disordered and amorphous carbon. *Phys. Rev. B* **61**, 14095 (2000).